

(2)

TECHNICAL REPORT BRL-TR-3175

**BRL**

AD-A230 289

PLASMA ANALYSIS OF A SMALL-BORE,  
ARC-ARMATURE RAILGUNALEXANDER E. ZIELINSKI  
JOHN D. POWELL

NOVEMBER 1990

DTIC  
ELECTE  
DEC 26 1990  
S B D  
C C

APPROVED FOR PUBLIC RELEASE; DISTRIBUTION UNLIMITED.

U.S. ARMY LABORATORY COMMAND

BALLISTIC RESEARCH LABORATORY  
ABERDEEN PROVING GROUND, MARYLAND

## NOTICES

Destroy this report when it is no longer needed. DO NOT return it to the originator.

Additional copies of this report may be obtained from the National Technical Information Service, U.S. Department of Commerce, 5285 Port Royal Road, Springfield, VA 22161.

The findings of this report are not to be construed as an official Department of the Army position, unless so designated by other authorized documents.

The use of trade names or manufacturers' names in this report does not constitute indorsement of any commercial product.

**UNCLASSIFIED**

REPORT DOCUMENTATION PAGE			Form Approved OMB No. 0704-0188	
<small>Public reporting burden for this collection of information is estimated to average 1 hour per response, including the time for reviewing instructions, searching existing data sources, gathering and maintaining the data needed, and completing and reviewing the collection of information. Send comments regarding this burden estimate or any other aspect of this collection of information, including suggestions for reducing this burden, to Washington Headquarters Services, Directorate for Information Operations and Reports, 1215 Jefferson Davis Highway, Suite 1204, Arlington, VA 22202-4302, and to the Office of Management and Budget, Paperwork Reduction Project (0704-0188), Washington, DC 20503.</small>				
1. AGENCY USE ONLY (Leave blank)		2. REPORT DATE November 1990	3. REPORT TYPE AND DATES COVERED Final, May 88 - Dec 89	
4. TITLE AND SUBTITLE  Plasma Analysis of a Small-Bore, Arc-Armature Railgun			5. FUNDING NUMBERS  PE: 61221A	
6. AUTHOR(S)  Alexander E. Zielinski and John D. Powell				
7. PERFORMING ORGANIZATION NAME(S) AND ADDRESS(ES)			8. PERFORMING ORGANIZATION REPORT NUMBER	
9. SPONSORING / MONITORING AGENCY NAME(S) AND ADDRESS(ES)  U.S. Army Ballistic Research Laboratory ATTN: SLCBR-DD-T Aberdeen Proving Ground, MD 21005-5066			10. SPONSORING / MONITORING AGENCY REPORT NUMBER  BRL-TR-3175	
11. SUPPLEMENTARY NOTES  Research Sponsored by: Close Combat Armaments Center, ATTN: SMCAR-CCL-FA, Picatinny Arsenal, NJ 07801-5001				
12a. DISTRIBUTION / AVAILABILITY STATEMENT  Approved for public release; distribution unlimited.			12b. DISTRIBUTION CODE	
13. ABSTRACT (Maximum 200 words)  Diagnostic measurements of plasma-armature properties have been made on a 9.3-mm square-bore, arc-driven railgun. The measurements include the total current carried by the arc, the voltages across the breech and muzzle ends of the gun tube, light output from the arc seen at points along the gun tube, and finally the time rate of change of the induction field associated with the armature current. From these data it is possible to infer the length of the arc and the current-density distribution within it as a function of time. The aggregate of this information is then used to provide input for a second mathematical model which allows deduction of the armature temperature, ionization state, pressure, and mass. Results of the data analysis are compared with those of one-dimensional steady-state theory and with conclusions from a recent 50-mm square-bore railgun experiment. The dissimilarities between the two experimentally derived results are noted, and possible reasons for those differences discussed.				
14. SUBJECT TERMS  Railgun, Plasma Armature, Electromagnetic Propulsion, Plasma Diagnostics, Electromagnetic Guns			15. NUMBER OF PAGES 33	
			16. PRICE CODE	
17. SECURITY CLASSIFICATION OF REPORT UNCLASSIFIED	18. SECURITY CLASSIFICATION OF THIS PAGE UNCLASSIFIED	19. SECURITY CLASSIFICATION OF ABSTRACT UNCLASSIFIED	20. LIMITATION OF ABSTRACT UL	

**UNCLASSIFIED**

INTENTIONALLY LEFT BLANK.

## Table of Contents

	<u>Page</u>
LIST OF FIGURES . . . . .	v
ACKNOWLEDGEMENTS . . . . .	vii
I. INTRODUCTION . . . . .	1
II. EXPERIMENT . . . . .	2
1. Diagnostic Probes . . . . .	3
2. Measured Data . . . . .	5
3. Inferred Data . . . . .	7
III. DATA-ANALYSIS MODEL AND SUMMARY OF EQUATIONS . . . . .	11
IV. RESULTS OF CALCULATIONS . . . . .	16
V. CONCLUSIONS . . . . .	22
REFERENCES . . . . .	25
APPENDIX . . . . .	27
DISTRIBUTION LIST . . . . .	29



<b>Accession For</b>	
NTIS GRA&I	<input checked="" type="checkbox"/>
DTIC TAB	<input type="checkbox"/>
Unannounced	<input type="checkbox"/>
Justification	
By _____	
Distribution/	
Availability Codes	
Dist	Avail and/or Special
A-1	



## List of Figures

<u>Figure</u>		<u>Page</u>
1	Axial locations of light sensors and B-dot probes. . . . .	4
2	Arc armature light detection circuit (one of four). . . . .	5
3	Measured plasma armature current as a function of time. . . . .	6
4	Measured muzzle voltage as a function of time. . . . .	7
5	Light sensor output voltage for three sensors as a function of time. . . . .	8
6	Measured B-dot probe output signal voltage (dotted curves) and calculated B-dot response (solid curves) for four sensors as a function of time. . . . .	8
7	Assumed current density distribution. . . . .	10
8	Spatial distribution of armature current density at four different times. . . .	10
9	Model for data-analysis calculations. . . . .	11
10	Average and peak temperature as a function of current. . . . .	17
11	Mean ion concentration as a function of current. . . . .	18
12	Arc mass as a function of time. . . . .	18
13	Arc length as a function of time. . . . .	19
14	Pressure as a function of position at $t \simeq 420 \mu s$ . . . . .	20
15	Current density as a function of position at $t \simeq 420 \mu s$ . . . . .	20
16	Temperature as a function of position at $t \simeq 420 \mu s$ . . . . .	21

INTENTIONALLY LEFT BLANK.



## **ACKNOWLEDGEMENTS**

The editorial comments and technical assistance contributed by Mr. Henry Burden in the preparation of this manuscript are gratefully acknowledged. Technical discussions with Dr. Keith A. Jamison, SAIC Inc, Shalimar FL, have been very helpful in understanding plasma armature behavior.

INTENTIONALLY LEFT BLANK.

# I. INTRODUCTION

In some recent work,<sup>1-3</sup> diagnostic measurements of plasma properties were made on the arc-driven railgun, CHECMATE, at Maxwell Laboratories. At that time CHECMATE, which has a square bore 50 mm on a side and which is about five meters in length, was the largest-bore railgun in operation. In this report we describe similar measurements undertaken on a smaller-bore gun, roughly 9.3 mm square, located at the Ballistic Research Laboratory (BRL). These measurements represent a part of our continuing effort to characterize plasma properties for launchers of various dimensions, and to understand how those properties affect gun performance.

Measurements to be discussed include the rail current and the voltage drops across the breech and muzzle ends of the gun, all as functions of time during the shot. In addition, several inductive sensors (B-dot probes), positioned at various points along the gun tube, provide data concerning the magnetic-induction field arising from current in the arc as it passes the point in question. The data from these probes are then analyzed to determine the location of the plasma arc and the spatial distribution of current density within it. Finally, data from fiber-optic probes located along the gun tube yield some information concerning light output from the arc incident on the insulator surfaces. This technique of inferring the armature current distribution and arc length from armature B-dot probe data was originally developed for 12.7-mm square-bore plasma armature characterization experiments.<sup>4</sup>

In addition to the above measurements and analyses, for CHECMATE an analytic model was developed to determine various properties of the arc that could neither be measured nor inferred directly from the experiment. Such properties included, for example, the temperature, the ionization state, the arc mass, and the pressure as a function of position in the arc. The model was based on the previously developed one-dimensional, steady-state theory of Powell and Batteh,<sup>5</sup> but several modifications were introduced in order to make best use of the experimental results. In particular, the temperature in the arc was inferred directly from the measured muzzle voltage and the experimentally determined current density. The direct use of experimentally derived quantities avoids assumptions regarding energy loss/gain mechanisms in the arc and undertaking reasonably difficult calculations based on energy conservation. Some purely theoretical calculations were performed, however, for purposes of comparison with results obtained from the data analysis.

In the present work, we have repeated for the 9.3-mm square-bore railgun both the experiment and the data analysis undertaken earlier for CHECMATE. Although there are similarities among the referenced plasma armature experiments, enough differences exist to prevent a rigorous comparison of the calculated results. For example, the peak magnetic-bore pressure was 2.5 times greater in the CHECMATE experiments than in either small-bore experiment. In the 12.7-mm experiment a stationary foil fuze and projectile was utilized, while in both the 9.3-mm and CHECMATE experiments the projectile was injected. Additionally, for the 9.3-mm experiments the plasma armature was pre-formed and injected. The rail material for the 12.7-mm and CHECMATE experiments was oxygen-free hardened copper (OFHC), whereas a copper-niobium (Cu-Nb) microcom-

posite material was used in the 9.3-mm experiments. Finally, the time dependence of the current waveforms for all the experiments was significantly different so that time dependent armature effects would preclude any quantitative comparisons.

The report is organized as follows. In Section II, the experiment is described briefly as well as the manner in which certain arc properties are inferred from the experimental data. In Section III, the governing equations for the data-analysis model are summarized. In Section IV, we describe in some detail the results of the data-analysis calculations, emphasizing where possible similarities and differences with the CHECMATE results. Finally, in Section V, we present our conclusions.

## II. EXPERIMENT

The work to be described here was undertaken primarily to test the resistance of various rail materials to arc ablation;<sup>6</sup> however, the diagnostics employed to quantify potential rail-damaging phenomena also accurately characterize the arc. The railgun was one meter long, had a bore cross section 9.3 mm square, and incorporated 305 mm long replaceable rail inserts at the breech end. The material which constituted the rail inserts was a copper-niobium microcomposite. The insulating side walls were composed of G-11, a fiberglass epoxy laminate. Near the breech a section of the side wall was instrumented with inductive coils (B-dot probes) which sense the time rate of change of the magnetic-induction field produced exclusively by the arc, and fiber-optic sensors (light pipes) which collect light from the arc. Additional diagnostics included measurements, via techniques to be described, of the breech and muzzle voltages, the time rate of change of the rail current, and the initial capacitor voltage. The barrel containment structure consisted of a pair of steel angles clamped along the axial length of the gun with six large C-clamps. The railgun had a measured inductance gradient of  $0.37 \mu\text{H/m}$ .

An electrothermal (ET) accelerator was used both to accelerate the projectile into the breech of the railgun and to form the main plasma arc. This injector contains an electrically exploded aluminum wire fed through a cylindrical polyethylene liner called a capillary. The ionized, low molecular weight plasma, composed mostly of carbon, was ejected from the capillary's open end and was used to drive the projectile into the railgun. Bore discontinuities between the injector and railgun limited the injection velocity to less than 200 m/s. Also, poor projectile sealing to the railgun bore surface allowed the low-density, high-temperature plasma to accelerate ahead of, i.e., to "blow-by", the projectile thus inhibiting the expected establishment of the main railgun arc. To insure an adequate conductive path behind the projectile, a 3 mg strip of aluminum foil with dimensions  $3.12 \text{ mm} \times 19.2 \text{ mm} \times 0.0254 \text{ mm}$  was glued to the rear of the projectile. The mass of the lexan projectile was nominally one gram for all shots.

The power supply connected to the railgun consisted of two parallel 50 kJ, 11 kV capacitors discharged through a  $1.7 \mu\text{H}$  pulse-shaping inductor. The main "on" and "crow-bar" switches were D-size ignitrons (NL5553). The injector power supply was a solid-state-switched, 2000 volt, three-element pulse forming network (PFN) capable of delivering 2500 amperes in  $250 \mu\text{s}$  to a matched load. The sequence of operation was initiated by charging

the main and ET capacitor banks to the desired voltages. The injector bank was triggered first and, after a pre-set time delay, the main bank was triggered. The arrival time of the arc armature into the railgun breech was the most unpredictable variable from shot to shot and was the largest contributor to variation in the initial arc start location.

We now describe the orientation and use of the various diagnostic probes, the specific measurements made, and how these measurements are used to derive the arc properties considered in Section I. The discussion here is intended to be summary; details concerning the procedures have been given in References 1, 2, and 4.

## 1. Diagnostic Probes

All electrical data were taken during the experiment using three Nicolet 4094C Digital Oscilloscopes. Most of the data were recorded at a rate of  $1 \mu\text{s}/\text{point}$  using 12 bit amplifiers ( $1 \text{ MegaSample/s}$ , amplifier model number 4562). The voltage data were recorded at the same rate using 8 bit amplifiers (model number 4175). The capacitive power supply utilized a single point grounding scheme with the signal cables in close proximity to the scope return ground braid. This positioning helps to avoid any induced loop currents in the data-signal lines. The data are stored on  $5\frac{1}{4}$ -inch floppy disks and later transferred to the large computer for further analysis.

The breech and muzzle voltages were sensed by a resistor string looped through a Pearson current transformer (model 110A). The twisted leads of the resistor string were connected directly across the potential to be measured. The transformer then sensed the current through the resistor string and produced a voltage proportional to the resistor current. The breech and muzzle resistor strings were  $486.0 \Omega$  and  $100.6 \Omega$  with D.C. power ratings of 60 and 100 watts, respectively. The Pearson current transformer's sensitivity of  $0.1 \text{ V/A}$  results in voltage divider ratios of 4860:1 for the breech, and 1006:1 for the muzzle. The transformer isolates the measuring devices from the experiment, precluding measuring-circuit grounding and voltage break-down dilemmas. However, care must be taken when using this technique with an injected ET plasma. Resistor strings in previous experiments were destroyed when injected gasses failed to reionize and the resistor string, offering the only discharge path, had to absorb the full capacitor bank energy.

Coils of wire (B-dot probes) are commonly used to generate a voltage associated with a changing magnetic field and thus to provide data from which the magnitude and orientation of the field can be inferred. In this experiment the coils were positioned along the length of the launcher, with coil and bore axes parallel in order to sense only the magnetic-induction field associated with the current through the arc armature. The first, third, and fourth coils each consisted of five turns of 30 gage wire, wrapped on a 4.89-mm diameter form; the remaining B-dot coil inadvertently had only four turns of wire. The computation of the B-dot sensor output voltage used in the computer code fitting routine<sup>4</sup> is based on the assumption that the coils are identical. The signal amplitude from the second coil was multiplied by  $\frac{5}{4}$  to compensate for the missing turn. The 5.00-mm thick G-11 insulator wall had a 2.54-mm recess in the outside face to accommodate each sense coil. This arrangement results in a bore-center to coil-center distance of 9.79 mm. The four coils used in the experiment were spaced at 61-mm intervals along the instrumented

insulating side-wall section. This section was so positioned, by addition of a 70-mm long G-11 spacer (see Figure 1), so that the moving armature would pass well within the sensing range of the first B-dot probe and slightly after peak current.

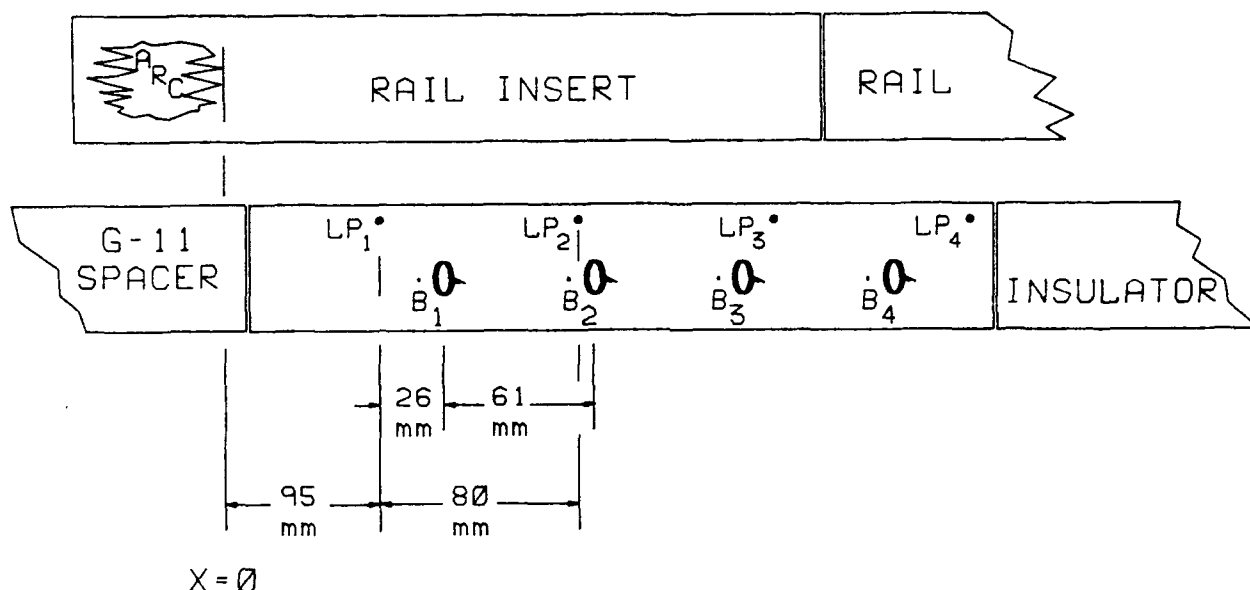


**Figure 1.** Axial locations of light sensors and B-dot probes. Light sensors are labelled by  $LP_1$  through  $LP_4$  and B-dot probes by  $B_1$  through  $B_4$ . All sensors and probes are centered between the rails.

In order to define the location of the front of the armature along the barrel length, light from the luminous part of the arc was detected by a reverse-biased pin-diode. The light signal was routed from the inner bore surface via 1.2-m of plastic, fiber-optic cable. The schematic for one light sensing circuit is shown in Figure 2. After each shot, the fiber-optic cable ends were removed, cleaned, and reglued into the insulator side wall. Along this section there were four fiber-optic sensors spaced at 80-mm intervals.

The railgun current typically rises to peak in about  $100 \mu s$ . With a waveform which varies this rapidly, it is advantageous to measure the time rate of change of the current and obtain the total current by either numerical or electronic integration. In addition, the  $di/dt$  signal does not mask functional anomalies as an integrated waveform may. Since the number of available scope channels was limited, we recorded the  $di/dt$  signal directly from a Rogowski coil, and performed the integration numerically using a five point smoothing algorithm. The Rogowski coil used for these experiments was fabricated and calibrated at BRL. Its conversion factor is  $28.7 \times 10^6 A/Vs$  and it has a rise time of less than  $3 \mu s$ .

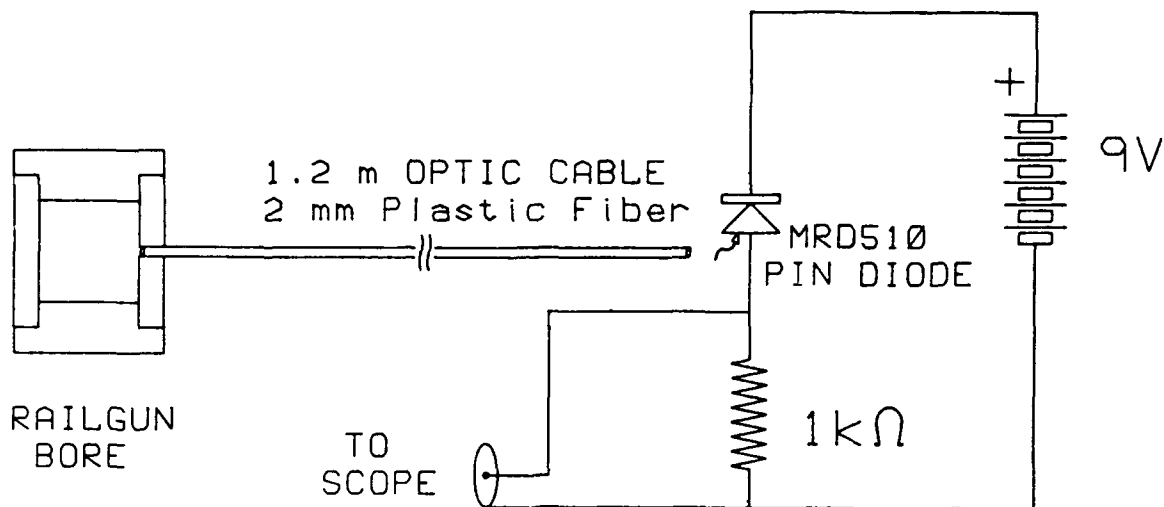


**Figure 2.** Arc armature light detection circuit (one of four).

## 2. Measured Data

There were four firings performed in this series of experiments. Only one shot, which corresponded to 8 kV of initial capacitor charge voltage, produced sensor data that could reasonably be reduced. For that case, arc initiation occurred 30 mm from the breech end of the conducting rail sample and 121 mm before the first B-dot probe. For the remaining shots, arc initiation occurred so late that B-dot data were obtained at or before peak current; thus the first station data had to be discounted. We believe that the elapsed time to arrival at the first B-dot station was too short to allow the use of the steady-state analysis. The remaining three data stations proved insufficient to establish the fitting parameters of the arc to the accuracy needed.

The armature current, shown in Figure 3, rises to its peak, 142.4 kA, at 106.5  $\mu$ s, well before the arc front has reached the first light sensor. The waveform is a consequence of "crowbarring" the capacitors to interrupt the RLC ringing that normally follows switch closure to the power conditioning inductor and load. Crowbarring forestalls damaging dielectric stress in the capacitor created by the voltage reversals that arise from circuit ringing. Ideally, a resistanceless short circuit would be placed across the capacitor just as its voltage (and energy) pass through zero, roughly coincident with current peak. In practice an ignitron crowbar switch was used whose nonzero resistance, in fact, drops to a few milliohms only after the voltage reversal has grown to 1200 volts. Though not harmful to the capacitor, this voltage reversal represents sufficient stored energy to promote a high frequency oscillation in the capacitor-crowbar circuit loop. Because the ignitron is common to both this loop and the gun circuit loop, its resistance and inductance couples energy between the two loops. The resultant, modulated armature current thus shows

a 30% drop from peak in 100  $\mu s$ , followed by 400  $\mu s$  of undulations after current peak. This waveform could not be satisfactorily fitted to a function and therefore the measured current waveform was used in the fitting routine.

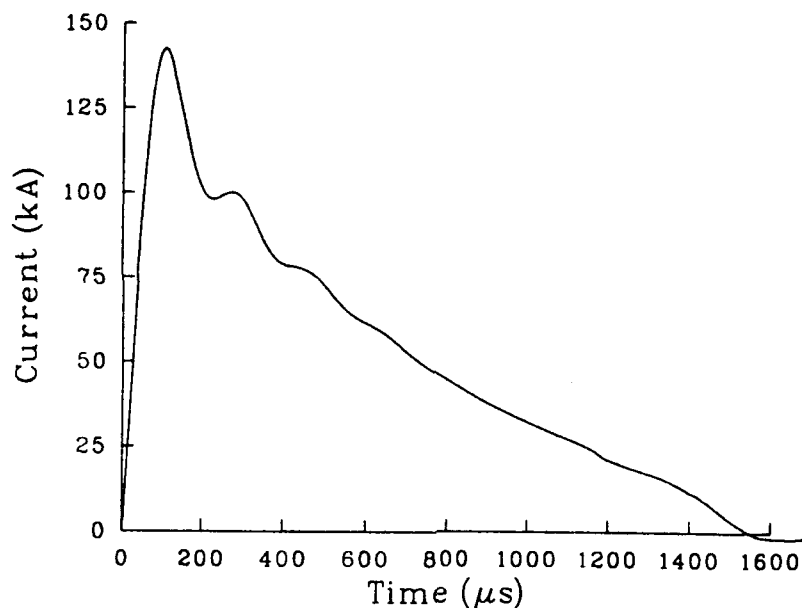


**Figure 3.** Measured plasma armature current as a function of time.

Figure 4 shows a trace of the measured muzzle voltage. The waveform is typical of all tests in this series of experiments. The first 5  $\mu s$  corresponds to vaporization of the aluminum foil strip and reheating of the ET plasma which cooled during injection. The shape of the muzzle voltage waveform prior to 200  $\mu s$  is indicative of rapid contraction (5-75  $\mu s$ ) and expansion (75-200  $\mu s$ ) of the plasma armature. For times greater than 200  $\mu s$ , the projectile and plasma armature are accelerated until they exit at the muzzle of the gun at 1140  $\mu s$ . The voltage drop across the armature is 150 volts for most of the acceleration time.

The pin-diode output for three light sensors, labelled  $LP_1$ ,  $LP_2$ , and  $LP_3$ , is shown in Figure 5. The nonzero signal output for the first light sensor at 305  $\mu s$  is indicative of plasma material running ahead of the projectile, alternatively known as blow-by. This presumably occurs because of inadequate sealing of the projectile to the inner surface of the bore. The arc front, characterized by the steady rise to maximum voltage in light sensor output, crossed the first sensor at 336  $\mu s$ . The arc front crossed the second and third light sensors at 414  $\mu s$  and 476  $\mu s$ , respectively. The plasma blow-by luminosity seen at these two probe locations is significantly less than that observed at the first probe. Although probe sensitivities differ, the differences in signal amplitude are nonetheless large enough to indicate that each subsequent decrease is real. Presumably, the decrease evident in the light signals preceding the sharp rise for each of the two sensors occurs because of cooling of the low-density plasma. The light sensor ( $LP_1$ ) nearest the breech shows that the bore is quite luminous even after the plasma armature has reached the muzzle end of the rails and all light sensors indicate a very erratic structure far behind the main plasma



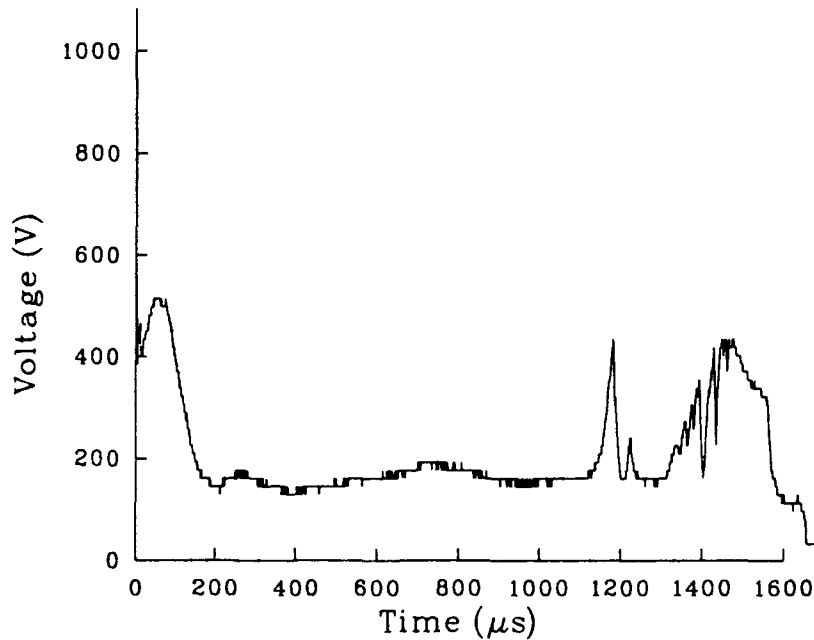


**Figure 4.** Measured muzzle voltage as a function of time.

armature. Data from the fourth sensor ( $LP_4$ ) were not included on the graph; a faulty data cable connector attenuated the signal to a level too small to be seen on the scale of the figure.

Figure 6 displays the four measured B-dot signals, indicated by dotted lines, while the solid lines are those calculated using the fitting procedure from Reference 4. The relative magnitude of the signals is difficult to interpret because of the perturbations in the decaying armature current discussed previously. The rapid fluctuations which appear throughout the signals evidently result from dynamic structure in the plasma armature and were not observed in the CHECMATE B-dot data. There is also some evidence that part of the current may at times be carried by parasitic conduction (termed "secondary-arc" or, when the conduction zone is well separated from the main arc, termed "restrike arc") behind the main plasma armature. Evidence for this behavior can be seen most clearly in data from the fourth B-dot probe at  $607 \mu s$  where a quasi-sinusoidal disturbance is superimposed on the main B-dot waveform. The exact location of the disturbance is not known but it appears from all the B-dot sensors that the disturbance is traveling with the arc, moving from the armature/projectile interface towards the breech as time progresses. It has been postulated that the formation of restrike arcs may be a serious obstacle in using railguns to achieve muzzle velocities higher than  $6 \text{ km/s}$ .<sup>7</sup>

### 3. Inferred Data

In References 1 and 2 it was explained how the data obtained via the methods described above could be used to infer properties of the arc that could not be measured

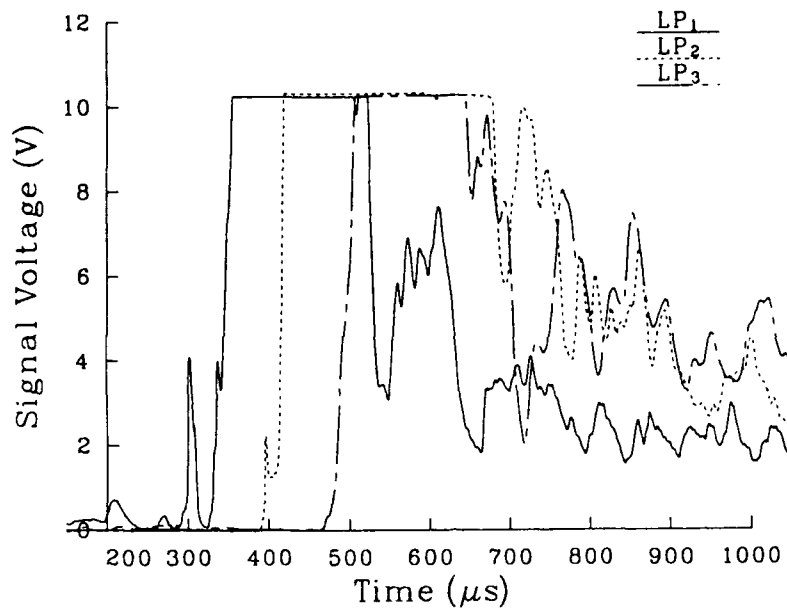


**Figure 5.** Light sensor output voltage for three sensors as a function of time.

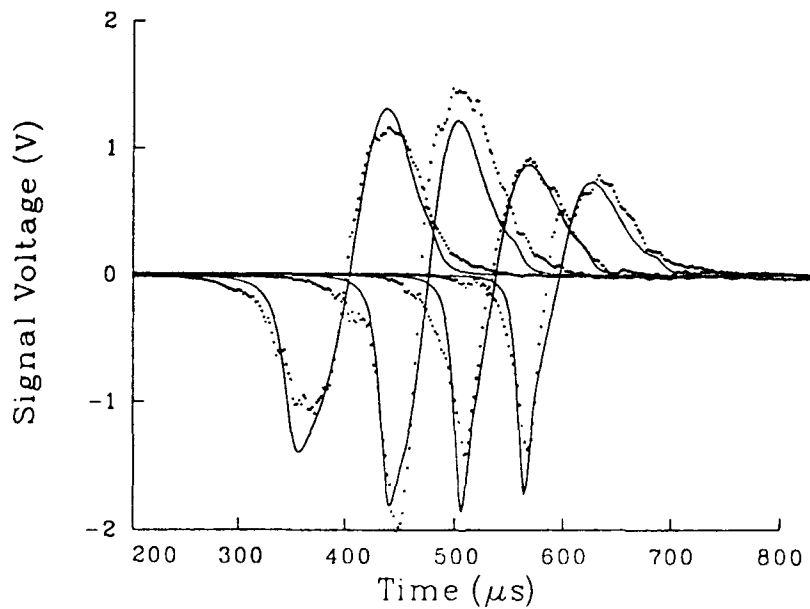


**Figure 6.** Measured B-dot probe output signal voltage (dotted curves) and calculated B-dot response (solid curves) for four sensors as a function of time.

directly. For the experiment under discussion here, the same basic procedure was followed except for two major differences. Here the actual current trace was used in all the data analyses, whereas for CHECMATE the current was fitted to an exponential decay. The unsmoothed current data were used directly in this analysis in order to account for the perturbations discussed earlier and to model the B-dot response as accurately as possible. Second, the time of negative peak voltage in three B-dot signals (numbers one, two, and four) and the time of muzzle exit were used to fit the arc front position to a third-order polynomial in time. The CHECMATE arc position was fitted to a polynomial in which the time of each negative peak in all four B-dot signals was used.

In the first phase of the analytic process the data were used to determine the current density in the arc. The technique consists of iteratively adjusting five constants of a computer-modeled, traveling spatial current-density distribution until its calculated magnetic-induction fields at the B-dot positions match the measured output signal voltage from the four B-dot coils. The goodness of fit is determined by minimizing the difference between the calculated and measured coil signals. The chosen current distribution had the functional form of the statistical Gaussian, adapted by truncating and removing one wing at a point near the peak, representing the rear of the projectile. The other point of truncation is somewhat arbitrary and, in the determination of the arc length, is the point where the current density has fallen to ten per cent of its peak value. The choice to use a Gaussian function was made because it produces current profiles that resemble those obtained theoretically,<sup>3</sup> and because it has proved successful in modelling the B-dot signals in previous work. A parametric description of the current density distribution,  $J(x, t)$ , is illustrated in Figure 7. The position of the distribution was carefully matched to the experimentally measured in-bore trajectory and, at any instant, the area integral of the distribution was held equal to the corresponding value of measured total current. The Biot-Savart integral was applied over the volume of the simulated arc to calculate the magnetic-induction fields.

In accord with the theoretical treatment, equilibrating times are considered short and we assume that the current distribution varies quasi-statically. Parametric relationships among space, time, and total rail current may be obtained from the measured current trace and the fitted position relationship. Because the fitting constants were determined by including the data from all four sensor stations, we assume that they describe the distribution anywhere between these stations. Thus a current density may be plotted for any of the points in time or position within the bounds of the data set employed. Figure 8 shows current-density distribution curves plotted at each of four positions indicating total armature currents of 60, 70, 80, and, 90 kA. We have, for illustrative purposes, truncated the arc length to correspond to the point where the current density was two per cent of its peak value. The arc length can be seen to be in the range of 120 - 80 mm for currents in the range 60 - 90 kA.

The length of the arc defined as the distance between the truncated points, (e.g.,  $X(t) - 3W(t)$ , see Figure 7), varies approximately inversely with the total current, and grows as the current decays. In the second phase of the analysis (Section III) the long, trailing end of the Gaussian, rather than being sharply truncated, is replaced by a short fillet that preserves continuity of the current density and its first derivative. Details concerning

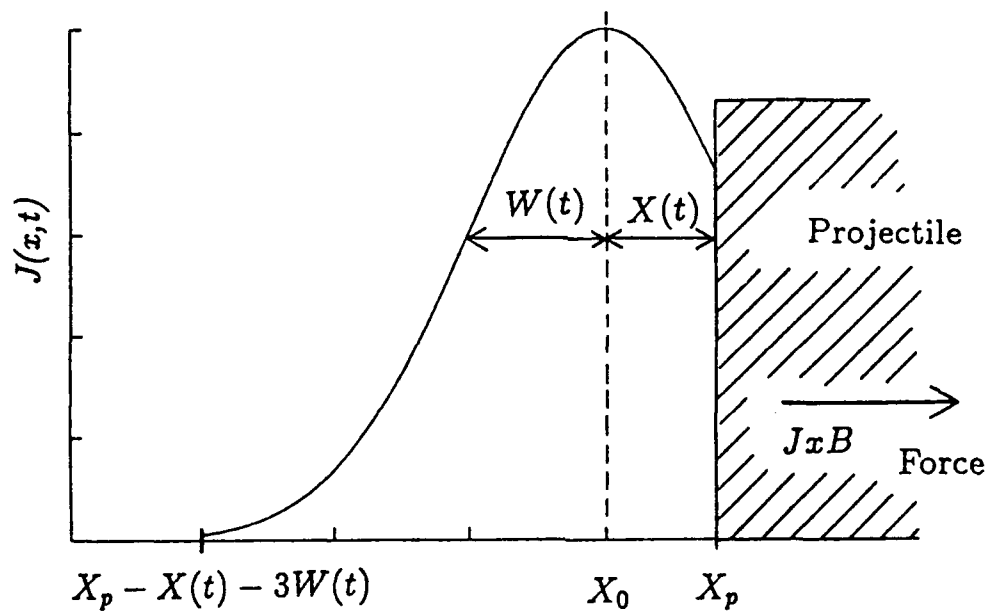


**Figure 7.** Assumed current density distribution.

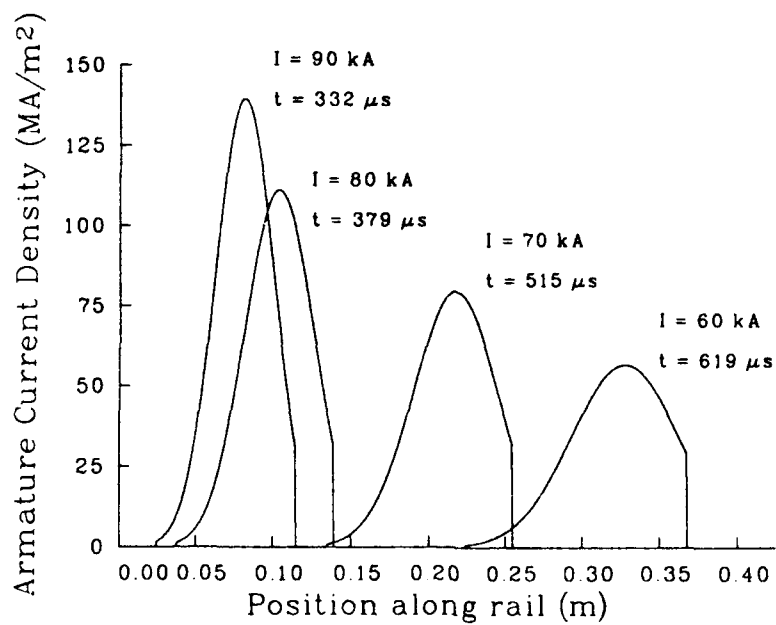


**Figure 8.** Spatial distribution of armature current density at four different times.

the fitting procedures as well as the determination of the arc length are in References 1 and 2.

Measured quantities and values derived in the first phase of analysis will now be used in the second phase of the analysis. The second phase of the data analysis via model calculations will be described in Section IV. Information measured in or derived directly from the experiment and required by this model is presented in the appendix. The information includes: time of observation,  $t$ ; current,  $i$ ; muzzle voltage,  $V_m$ ; arc length,  $\ell_a$ ; projectile position,  $x_p$ ; half width,  $W$ , of the Gaussian; and distance,  $X$ , from the projectile to the peak in the Gaussian.

### III. DATA-ANALYSIS MODEL AND SUMMARY OF EQUATIONS

In this section we present the basic assumptions employed in the data-analysis calculations as well as the pertinent governing equations. Most of this information has been presented elsewhere <sup>1,3</sup> and is discussed here in summary fashion. A schematic diagram of the railgun is shown in Figure 9. Current is conducted along the rails (upper and lower sides in the figure) in the direction shown by the arrows and through a plasma arc confined between  $x = x_b$  and  $x = x_p$ . These positions denote, respectively, the back of the arc and the projectile surface measured relative to the breech end of the railgun. As in previous work, the rails are assumed to be perfect conductors and are separated along the  $y$  direction by a distance  $w$ .

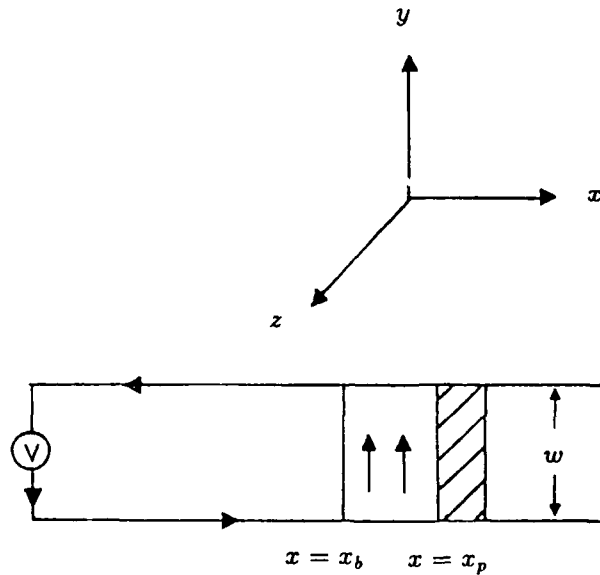


**Figure 9.** Model for data-analysis calculations.

Input provided by or derived from the experiment which are necessary to undertake the calculations are the muzzle voltage, pulsed current, projectile position, and arc length (determined by truncating the trailing end of the Gaussian at ten per cent of peak current density) all as a function of time during the shot. In addition, the location of the peak in the current density as well as the half width of the assumed Gaussian form, also derived from the experiment, are used directly in the model calculations. As indicated before, these data are presented in tabular form in the appendix.

Over most of the arc we assume, as in the fitting procedure, that the current density at any time can be represented by

$$J = \frac{1}{C_N} \exp \left[ -\frac{(x - x_0)^2}{2W^2} \right]. \quad (1)$$

The location of the maximum  $x_0$  is given in terms of the data in the appendix by  $x_0 = x_p - X$ . At the very back of the arc, however,  $J$  has been adjusted to go smoothly to zero in keeping with assumptions of previous theoretical models.<sup>5</sup> Specifically, we have represented the current density in this region by a quadratic function which vanishes at  $x = x_b$ . It is convenient in further analysis to define a dimensionless distance  $\xi$  by the relation

$$\xi = \frac{x - x_b}{\ell_a}, \quad (2)$$

where  $\ell_a$  denotes the arc length, namely,  $x_p - x_b$ . In this notation, then, the current density can be written

$$J(\xi) = \frac{1}{C_N} \exp \left[ -\frac{(\xi - \xi_0)^2}{2W_0^2} \right], \quad \xi > \xi^* \quad (3)$$

and

$$J(\xi) = A_1 \xi + B_1 \xi^2, \quad \xi < \xi^*. \quad (4)$$

The constant  $\xi^*$  can be chosen arbitrarily but should be small; in all subsequent calculations we have taken  $\xi^* = 0.1$ .

The parameters  $\xi_0$  and  $W_0$  are given by

$$\xi_0 = \frac{x_0 - x_b}{\ell_a} \quad (5)$$

and

$$W_0 = W/\ell_a; \quad (6)$$

the constants  $C_N$ ,  $A_1$ , and  $B_1$  follow from the requirement that  $J$  be normalized to the total current  $i$  at all times and that  $J$  and its derivative with respect to  $\xi$  be continuous at  $\xi = \xi^*$ . One obtains the following relations

$$C_N = \frac{[4W_0^2 + \xi^*(\xi^* - \xi_0)]\ell_a \xi^*}{6jW_0^2} \exp \left[ -\frac{(\xi^* - \xi_0)^2}{2W_0^2} \right] + \left( \frac{\pi}{2} \right)^{1/2} \frac{W_0 \ell_a}{j} \times \left[ \operatorname{erf} \left( \frac{1 - \xi_0}{\sqrt{2}W_0} \right) - \operatorname{erf} \left( \frac{\xi^* - \xi_0}{\sqrt{2}W_0} \right) \right], \quad (7)$$

$$A_1 = \frac{1}{C_N} \left[ \frac{2}{\xi^*} + \frac{(\xi^* - \xi_0)}{W_0^2} \right] \exp \left[ -\frac{(\xi^* - \xi_0)^2}{2W_0^2} \right], \quad (8)$$

and

$$B_1 = -\frac{1}{C_N \xi^*} \left[ \frac{1}{\xi^*} + \frac{(\xi^* - \xi_0)}{W_0^2} \right] \exp \left[ -\frac{(\xi^* - \xi_0)^2}{2W_0^2} \right]. \quad (9)$$

In these relations,  $j$  represents the current per unit height on the rail surface and  $\operatorname{erf}$  is the error function

$$\operatorname{erf}(x) = \frac{2}{\sqrt{\pi}} \int_0^x e^{-u^2} du. \quad (10)$$

From the derived current density represented by Equations (3) and (4), we can obtain the magnetic-induction field and pressure within the arc from results derived in Reference 5. Specifically, we have

$$B(\xi) = \mu^* j - \mu^* \ell_a \int_0^\xi J(\xi) d\xi. \quad (11)$$

In the above equation  $\mu^*$ , as discussed in Reference 5, is an effective magnetic permeability used to account approximately for the finite height of the rails. In terms of the real magnetic permeability  $\mu$ ,  $\mu^*$  is given by Battch's formula <sup>8</sup>

$$\mu^* = \frac{2\mu}{\pi S} \left[ S \tan^{-1}(S) + \frac{S^2}{4} \log(1 + 1/S^2) - \frac{1}{4} \log(1 + S^2) \right], \quad (12)$$

where  $S = h/w$ , i.e., the ratio of the rail height to the rail separation.

Equation (11), with aid from (3) and (4), can be integrated to produce

$$B(\xi) = \mu^* j - \mu^* \ell_a (A_1 \xi^{*2}/2 + B_1 \xi^{*3}/3) - \frac{\mu^* \ell_a W_0}{C_N} \left(\frac{\pi}{2}\right)^{1/2} \\ \times \left[ \operatorname{erf} \left( \frac{\xi - \xi_0}{\sqrt{2} W_0} \right) - \operatorname{erf} \left( \frac{\xi^* - \xi_0}{\sqrt{2} W_0} \right) \right], \quad \xi > \xi^*, \quad (13)$$

and

$$B(\xi) = \mu^* j - \mu \ell_a (A_1 \xi^2/2 + B_1 \xi^3/3), \quad \xi < \xi^*. \quad (14)$$

Similarly, it follows from the standard steady-state, momentum-conservation equation that the pressure as a function of position in the arc is given approximately by

$$P = \frac{\mu^* j^2}{2} - \frac{B^2}{2\mu^*}. \quad (15)$$

Equation (15) holds only when the arc mass is small compared to the projectile mass, a condition that will be seen to prevail in all cases to be considered.

From the measured muzzle voltage  $V_m$  and the inferred current density represented by Equations (3) and (4), one can also calculate the electrical conductivity in the arc as a function of position. It has previously been proved,<sup>9</sup> neglecting the rail's resistive contribution, that in the steady-state the quantity  $J/\sigma$  is constant within the arc and that its value is given by

$$J/\sigma = V_P/w. \quad (16)$$

Here  $\sigma$  represents the arc conductivity and  $V_P$  represents the potential drop across the plasma. In order to make use of this condition it is obviously necessary to make some assumption regarding the relationship between the measured muzzle voltage and the potential  $V_P$ . Evidently, one has

$$V_P = V_m - V_c, \quad (17)$$

where  $V_c$  is the total contact potential at the rail-arc interfaces. Unfortunately, reliable estimates of  $V_c$  are not known, but we will discuss results for various estimates.

The remaining properties of the arc that require calculation are the ionization state, the temperature, and finally the density. We will account only for first ionization in the remainder of the analysis since the relevant temperatures are sufficiently low that higher ionization states are negligible. If we denote by  $x_1$  the ratio of ions to heavy particles (ions and neutrals) in the plasma, then  $x_1$  must satisfy the Saha equation

$$\frac{x_1^2}{1 - x_1^2} = \frac{2}{P} \frac{Z_1}{Z_0} \left( \frac{m_e}{2\pi\hbar^2} \right)^{3/2} (k_b T)^{5/2} e^{-I/k_b T}. \quad (18)$$



Here,  $m_e$  denotes the electron mass,  $k_b$  Boltzmann's constant,  $\hbar$  Planck's constant divided by  $2\pi$ , and  $T$  the temperature. The constant  $I$  is the first ionization potential of the material which constitutes the arc and the  $Z$ 's are electronic partition functions whose ratio can be approximated by unity or whose values can be computed from tables.<sup>10</sup>

The electrical conductivity of the arc can be approximated by the expression

$$\frac{1}{\sigma} = \frac{1}{\sigma_L} + \frac{1}{\sigma_H} \quad (19)$$

where  $\sigma_L$  denotes the conductivity of a weakly ionized gas in which electron-neutral collisions dominate, and  $\sigma_H$  that for a highly ionized gas in which electron-ion collisions are important. For  $\sigma_L$ , we use the relation

$$\sigma_L = \frac{4.5 \times 10^{-12} x_1}{(1 - x_1) Q T^{1/2}} \quad (20)$$

where  $Q$  is the electron-neutral scattering cross section. Equation (20) was derived from standard expressions involving the neutral concentration and the mean electron thermal velocity. All units are MKS so that the conductivity obtained in this expression is in mho/m. For  $\sigma_H$  we use the Spitzer relation for single ionization which can be written

$$\sigma_H = 1.53 \times 10^{-2} T^{3/2} / \log \Lambda \quad (21)$$

where  $\Lambda$  is given by

$$\Lambda = 4.56 \times 10^{-5} T^{5/2} \left( \frac{1 + x_1}{x_1 P} \right)^{1/2}, \quad (22)$$

again in MKS units. These relationships for the conductivity and ion concentration are sufficient to determine  $x_1$  and  $T$  provided the value of  $\sigma$ , obtained in Equation (16), is employed. Unfortunately, these relations cannot be solved for  $x_1$  and  $T$  explicitly and an iterative numerical technique must be used. Once the values are known, however, the arc density can be obtained from the assumed equation of state

$$\rho = \frac{m_0 P}{(1 + x_1) k_b T}, \quad (23)$$

where  $m_0$  is the mass of the ions or neutrals which make up the arc. Furthermore, the arc mass then follows by simply integrating the density, viz.,

$$m_a = h w \ell_a \int_0^1 \rho(\xi) d\xi. \quad (24)$$

## IV. RESULTS OF CALCULATIONS

We have used the formalism described in the preceding section to calculate a number of plasma arc properties, neither directly measurable nor easily inferred from the data, for the small-bore railgun shot described in Section II. All input data needed in the calculations were described previously and were taken from the available experimental data given in the appendix. In order to proceed with the calculations, it is also necessary to make assumptions concerning the constituency of the arc, since the plasma material is not known with any certainty. In our previous analysis of the large-bore, CHECMATE data we assumed for the most part that the arc was composed of carbon atoms and ions. However, some calculations were undertaken for both aluminum and copper-vapor arcs and results were found to be qualitatively similar to the carbon calculations. These additional choices were made because the rails were copper, the wire used to initiate the arc was aluminum, and the insulating rails were assumed to be composed primarily of carbon and hydrogen. Qualitatively, the various choices produced similar results and we will confine our attention here to only carbon arcs. We have, as before, also assumed negligible contact potential at the rail-arc interfaces except in cases where otherwise noted.

The calculations to be discussed are basically of two types. In the first, certain position-independent or average properties of the plasma are computed as a function of time or current; in the second, position-dependent quantities are calculated at a time when substantial agreement between calculated and sensor response is obtained. We now discuss some of the results, emphasizing in particular how they compare with results of the large-bore computations. Material properties of carbon used in all the calculations were:  $m_0 = 12 \text{ amu}$ ,  $Q = 2.7 \times 10^{-19} \text{ m}^2$ , and  $I = 11.26 \text{ ev}$ .

Shown in Figure 10 are the average and peak temperatures within the arc as a function of the current during the time of the shot. These results exhibit much the same behavior as for the large-bore gun. The increase in temperature with increasing current obviously arises from the more significant ohmic heating at higher currents. The temperatures are, however, lower by about a factor of two than for the large-bore case. This effect might be expected since the current in the small-bore shot was about an order of magnitude lower than that observed in the CHECMATE shots, while the bore height is only about five times smaller. The very marked increase in temperature at about 80 kA appears to result from mass blowing by the projectile at this time ( $t \simeq 400 \mu\text{s}$ ). This loss of both mass and current carriers causes higher energy loss into less material so that temperature rises to a new equilibrium. Evidence for this occurrence was discussed with regard to the light sensor data in Figure 5 and will be seen again when the arc mass as a function of time is presented in Figure 12. Apparently, the sudden loss in mass results in a decrease in density and consequent rise in temperature. It should be pointed out, however, that since this loss occurs on such a small time scale, the arc is probably not able to readjust immediately to the quasi-static state assumed in the data analysis. Therefore, quantitatively accurate results for all the flow variables may not be obtained during this time. For example, both blow-by and secondary-arc formation may correspond to rapid mass loss from the arc, the former occurring at the front and the latter at the back. Though these processes are remarkably different and can be expected to affect the arc in vastly different ways, the data-analysis calculations do not differentiate between the two occurrences.

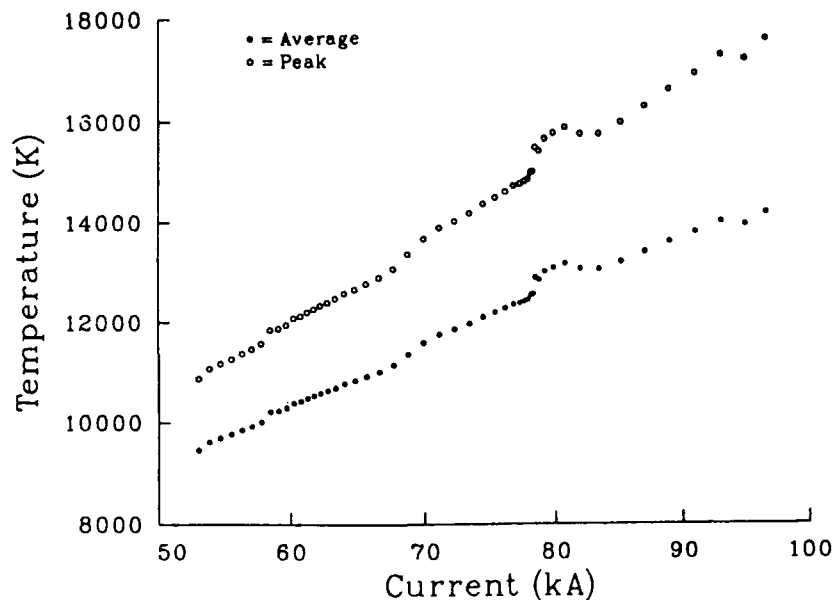


**Figure 10.** Average and peak temperature as a function of current.

Similarly, the mean ion concentration, shown as a function of current in Figure 11, shows trends similar to those observed in CHECMATE. The increase in ion concentration with increasing current results from the consequent increase in temperature. It should be observed, however, that even at the highest currents only about 15 per cent of the carbon atoms are ionized. In the CHECMATE case, significantly more ionization occurred, with the corresponding figure being about 50 per cent.

The arc mass,  $m_a$ , is shown as a function of time in Figure 12. There is a fairly significant drop in the mass at about  $400 \mu s$ , corresponding to a time when the fiber-optic data indicated light ahead of the projectile (see Figure 5). Thus, it appears that the mass decrease results from blow-by. Subsequent mass losses also correspond to precursor light data, although these perturbations are not so pronounced as that at  $400 \mu s$ . A similar effect was observed in some of the CHECMATE data and here, as for that case, this rapid, large-scale mass loss seems to be quickly restored. For this small-bore data, however, it is obvious that there is a gradual decrease in arc mass during the course of the shot. The loss is fairly small, only about ten per cent, but still significant as observed in the figure. No such effect was found in the CHECMATE data where, for all shots studied, the mass remained nearly constant during the time of the shot. The reason for the overall loss for the small-bore experiment is not entirely clear. One possible explanation could be the diffusion of neutrals out the back of the arc, a mechanism proposed by Barber<sup>11</sup> and discussed in References 1 and 3. In the small-bore gun there are obviously far more neutrals near the rear of the arc than in CHECMATE, perhaps too many to be carried along with the arc, and the temperature may be too low to ablate enough material from the insulators to make up for the loss.

The arc length as a function of time is shown in Figure 13. Data for this graph

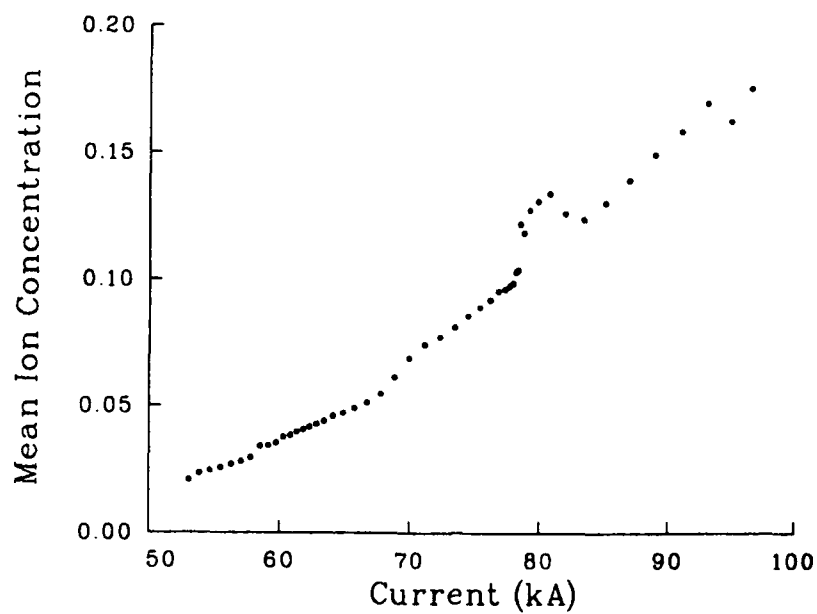


**Figure 11.** Mean ion concentration as a function of current.

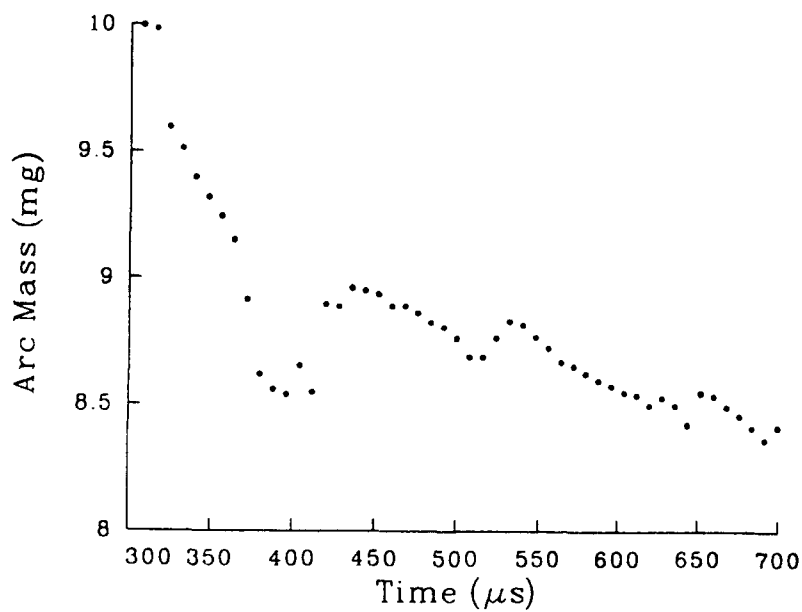


**Figure 12.** Arc mass as a function of time.

were taken directly from columns one and four of the table in the appendix. The arc becomes longer with increasing time primarily because the decreasing current exerts less of a compressive force. The near flattening of the curve between 400  $\mu s$  and 450  $\mu s$  results from the nearly constant current during this time interval (see Figure 3).

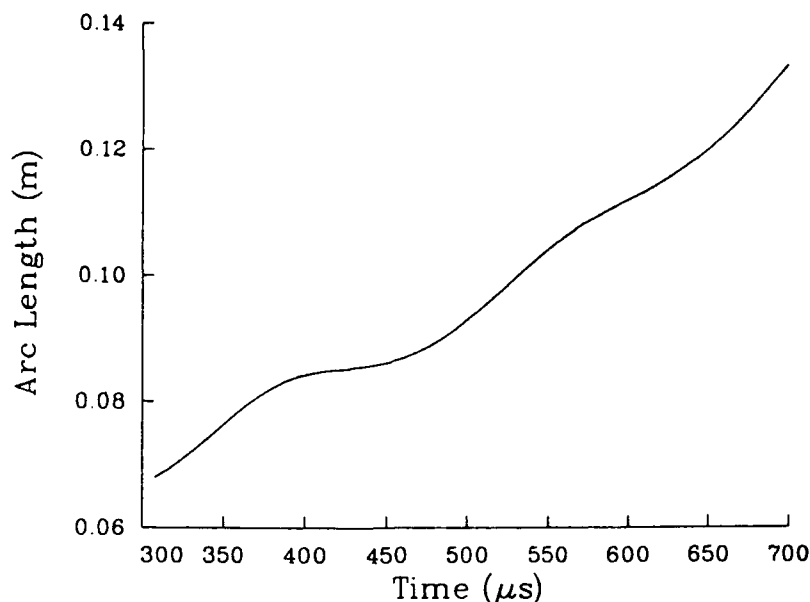


**Figure 13.** Arc length as a function of time.

Typical of position-dependent quantities in the arc are the pressure and current density shown in Figures 14 and 15. Both curves were calculated from the data at time  $t \simeq 420 \mu s$  when the current was about 78 kA (see data in the appendix) and when the fit of the calculated B-dot signal matched well with the experimentally measured signal. The pressure profile is similar to the theoretical curves we obtained in References 1 and 2. However, the magnitude of the pressure is lower than that observed at high currents in the CHECMATE shots, typically by a factor of about five. It is noteworthy that the current density reaches a peak considerably farther back toward the breech of the gun than in the CHECMATE case, where the peak occurred around  $\xi = 0.8$ . Presumably, the difference in peak locations can be attributed to the lower pressure associated with the small-bore shot and resulting longer radiation mean free path near the projectile surface. As has been pointed out previously, the magnitude of the temperature gradient near the projectile surface increases with decreasing mean free path. Thus, one would expect the temperature peak, and consequently the conductivity and current-density peaks, to occur closer to the projectile as the mean free path decreases.

We have also undertaken some purely theoretical calculations and, as in the case of CHECMATE, compared the output with results from the data analysis. The theoretical calculations were undertaken with our previously developed one-dimensional, steady-state model,<sup>5</sup> modified so that the computed temperatures were scaled downward by the factor  $(A_E/A_A)^{1/4}$ , where  $A_E$  was the surface area of the ends of the arc and  $A_A$  was the total

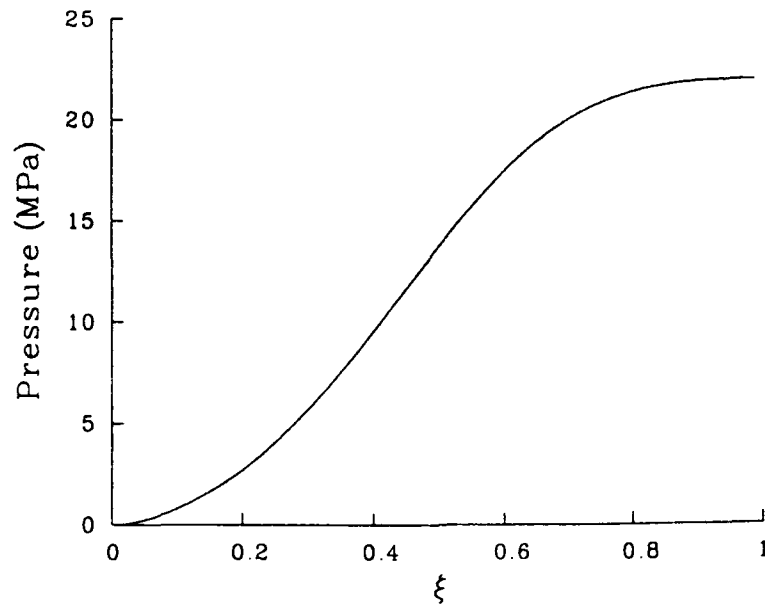


**Figure 14.** Pressure as a function of position at  $t \simeq 420 \mu s$ .

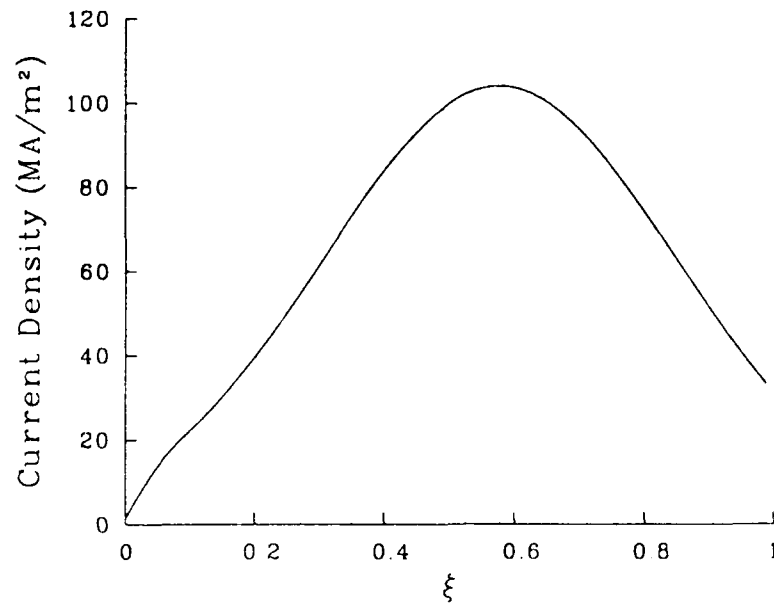


**Figure 15.** Current density as a function of position at  $t \simeq 420 \mu s$ .

surface area. As pointed out in Reference 1, this scaling was undertaken to account very approximately for the fact that radiation occurs from all sides of the plasma, not just from the ends as assumed in our original calculations. Various approximations are possible to account for radiation from all sides, but this simple scaling is the easiest to carry out and seems to give fairly reasonable results.

Shown in Figure 16, Curve A, is the theoretical temperature profile obtained when the current was about 78 kA and the arc length 85.1 mm, i.e., at the same point as for the current density and pressure shown in Figures 14 and 15. Only arc length and current need be supplied for the theoretical calculations. The profile looks somewhat different from those we have observed either in our previous theoretical calculations or in the theoretical calculation done for the CHECMATE data. In particular, the temperature gradient near the projectile is much smaller than in those other cases and the temperature maximum is located much closer to the breech end of the gun. As was discussed relative to the current-density curve in Figure 15, this behavior can presumably be ascribed to the longer radiation mean free path near the projectile surface associated with this small-bore shot.

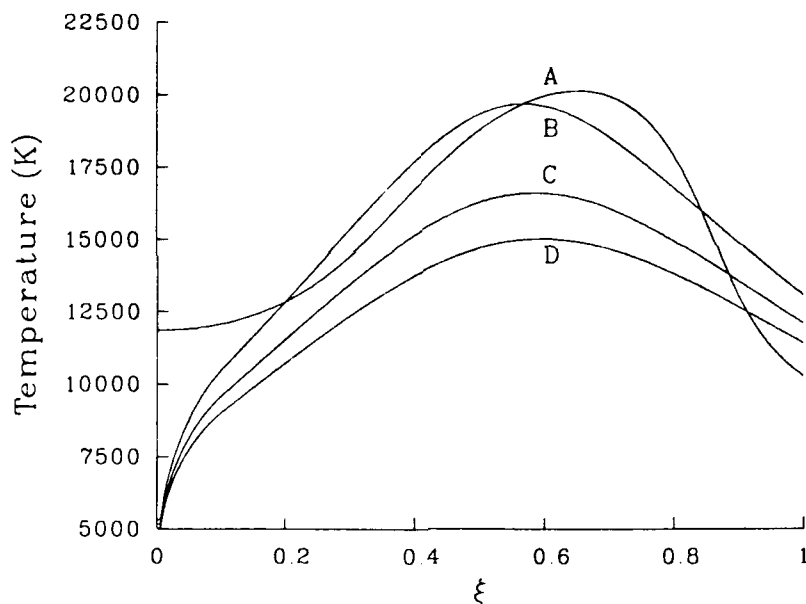


**Figure 16.** Temperature as a function of position at  $t \simeq 420 \mu s$ . A, theory; B, data analysis for  $V_c = 66.1$  volts; C, data analysis for  $V_c = 35$  volts; D, data analysis for  $V_c = 0$ .

The theoretical calculations do not, of course, account for any contact potential at the rail-arc interfaces. Therefore, as discussed in Reference 1, if we wish to compare the arc properties calculated theoretically with those obtained via analysis of the experimental data, it is necessary to subtract the contact potential from the measured muzzle voltage before undertaking the data-analysis calculations. Unfortunately, the magnitude of the contact potential is not known and, thus far, we have assumed it to be zero. We have, however, analyzed the data for various assumed contact potentials in an effort to get better agreement between theory and experiment. Results of these calculations are shown

**Table 1.** Comparison of Theoretical Results with Experimental Results for Different Contact Potentials

	<i>A</i>	<i>B</i>	<i>C</i>	<i>D</i>
$V_m(\text{volts})$	—	141.7	141.7	141.7
$V_c(\text{volts})$	—	66.1	35.0	0
$V_P(\text{volts})$	75.6	75.6	106.7	141.7
$m_a(\text{mg})$	6.85	6.06	7.72	8.89
$\langle T \rangle (K)$	15800	15600	13700	12600
$T_{max}(K)$	20100	19700	16600	15000
$\langle x_1 \rangle$	0.33	0.33	0.17	0.10

in Figure 16, Curves B, C, and D, and summarized in Table 1.

As is evident in Figure 16, the theoretical results of Curve A differ substantially from the data-analysis results of Curve D, computed for zero contact potential. In fact, the temperature peak in Curve A is about 35 per cent higher than that observed in Curve D. As the assumed contact potential increases, however, indicated by Curves B and C, the experimental and theoretical results are seen to be in better agreement. The increase in the mean temperature with increasing contact potential results from the consequent smaller values of  $V_p$ . These smaller values can result only if the conductivity and, thus, the temperature increase. The value of  $V_c$  in Curve B, namely, 66.1 volts was chosen so that the potential drop across the plasma,  $V_P$ , was the same as that calculated in the theoretical model [see Equation (17)]. For this assumption the two profiles are in reasonably good agreement. Other results from the various calculations are summarized in Table 1. As is evident results from A and B are in reasonable agreement except possibly for the arc mass where the disparity between the two calculations is about ten per cent. The contact potential is 47% of the measured muzzle voltage for this small-bore shot, whereas for CHECMATE it was 58%.

## V. CONCLUSIONS

The analysis of the data undertaken for the small-bore railgun has produced some results which are different from those obtained in the CHECMATE case. Most noteworthy are the decrease in arc mass during the time of the shot and the peaking of current density at a point farther removed from the projectile surface. The results have been tentatively interpreted as a consequence of the lower temperature and pressure associated with the plasma armature in the small-bore case. More analysis, however, both theoretical and experimental, seems in order.

As in the CHECMATE case, the temperatures obtained via the data analysis are still significantly lower than those obtained theoretically, unless a substantial contact potential at the rail-arc interfaces is postulated. It is conceivable, however, that some energy-loss



mechanism not accounted for in the theoretical models is responsible, at least in part, for the lower temperatures.

The composition of the arc still remains unknown. In the analyses undertaken here the plasma was assumed to be composed of carbon neutrals and ions only; computational experience has shown that even if a more precise mix of all the plausible constituents were used the qualitative results and conclusions would not be significantly altered.

Finally, we conclude that there is nothing in this analysis that would seem to preclude the use of plasma armatures in small-bore railguns. A similar conclusion was reached with regard to large-bore guns when analysis of the CHECMATE data was undertaken. There are, however, some modifications in both the experiment and the data analysis that would probably lead to more quantified conclusions. First, it is apparent from the muzzle voltage, B-dot traces, and light sensor traces that the arc at times exhibits very rapid fluctuations not observed in the CHECMATE case. Consequently, there are likely to be variations in its properties that occur on a time scale which is too small to make the assumption that the arc is quasi-static valid. Future attempts at analyzing data with this much variability would probably best be carried out, at least in part, with a fully time-dependent model. The adequacy of the quasi-static assumption could then be investigated. Second, it would seem desirable to use a greater number of more closely spaced sensors in order to define precisely the armature/projectile interface. This modification would allow use of a higher-order polynomial to fit the projectile trajectory and hence a more accurate determination of the armature acceleration. Third, use of insulating side walls that had not been drilled through completely would avoid saturation of the reverse-biased pin-diode. Fourth, a better system of sensing the armature in the railgun breech would insure arc initiation before the armature had reached the sensor arrays. This would provide a larger data set from which to compare the experimental results and ensure accurate determination of the inferred armature quantities. Finally, additional data channels permitting, supplemental diagnostic probes, such as rail magnetic-induction field sensors and a magnetic flux loop for sensing armature velocity, would aid in the explanation of some time-dependent effects.

INTENTIONALLY LEFT BLANK.

## References

1. Jamison, K. A., Burden, H. S., and Powell, J. D., "Plasma Properties of a Large-Bore, Arc-Armature Railgun," US Army Ballistic Research Laboratory Report Number BRL-TR-3014, July 1989.
2. Jamison, K. A. and Burden, H. S., IEEE Trans. Magn. MAG-25, 256 (1989).
3. Powell, J. D., IEEE Trans. Magn. MAG-25, 448 (1989).
4. Jamison, K. A., Marquez-Reines, M., and Burden, H. S., IEEE Trans. Magn. MAG-20, 403 (1984).
5. Powell, J. D. and Batteh, J. H., J. Appl. Phys. 52, 2717 (1981).
6. Renaud, C. V. and Zielinski, A. E., "Erosion Resistance of CuNb Microcomposites in a Plasma Armature Electromagnetic Launcher," J. Material Research, in review.
7. Parker, J. V., "Why Plasma Armature Railguns Don't Work (And What Can Be Done About It)," IEEE Trans. Magn. MAG-25, 418 (1989).
8. Batteh, J. H., J. Appl. Phys. 56, 3182 (1984).
9. Powell, J. D. and Jamison, K. A., "One-Dimensional, Time-Dependent Model for Railgun Arcs," US Army Ballistic Research Laboratory Report Number BRL-TR-2779, February 1987.
10. Moore, C. E., "Atomic Energy Levels," Nat. Bur. Stand. U. S. Circ. 467 (1952).
11. Barber, John P., private communication.

INTENTIONALLY LEFT BLANK.

# APPENDIX

$t(\mu s)$	$i(kA)$	$V_m(volts)$	$\ell_a(cm)$	$X(cm)$	$W(cm)$	$x_p(cm)$
307.7	96.70	152.8	6.80	3.206	1.673	10.11
315.8	95.01	154.8	6.92	3.233	1.719	10.46
323.8	93.10	145.7	7.07	3.264	1.773	10.83
331.8	91.07	145.7	7.24	3.298	1.834	11.22
339.7	89.02	144.7	7.41	3.334	1.900	11.64
347.8	87.04	144.7	7.59	3.370	1.967	12.08
355.8	85.17	144.7	7.77	3.404	2.034	12.54
363.8	83.48	143.7	7.94	3.437	2.098	13.03
371.8	82.02	137.7	8.09	3.466	2.155	13.54
379.8	80.82	129.6	8.22	3.490	2.205	14.06
387.8	79.90	128.6	8.32	3.509	2.244	14.61
395.8	79.23	128.6	8.40	3.523	2.273	15.18
403.8	78.77	132.7	8.45	3.533	2.294	15.77
411.8	78.48	129.6	8.49	3.539	2.307	16.38
419.8	78.29	141.7	8.51	3.543	2.316	17.01
427.7	78.12	141.7	8.53	3.546	2.323	17.65
435.8	77.91	144.7	8.56	3.551	2.333	18.32
443.8	77.65	144.7	8.59	3.557	2.345	19.00
451.8	77.28	144.7	8.63	3.565	2.362	19.69
459.8	76.78	143.7	8.69	3.575	2.386	20.40
467.8	76.15	144.7	8.78	3.589	2.416	21.13
475.7	75.38	144.7	8.88	3.607	2.455	21.87
483.8	74.46	144.7	9.00	3.628	2.502	22.63
491.8	73.42	145.7	9.14	3.652	2.556	23.40
499.8	72.29	145.7	9.30	3.679	2.618	24.18
507.8	71.12	144.7	9.47	3.707	2.684	24.98
515.8	69.95	146.7	9.65	3.737	2.754	25.78
523.7	68.81	152.8	9.83	3.766	2.824	26.60
531.8	67.72	158.8	10.01	3.794	2.895	27.43
539.8	66.67	160.8	10.19	3.822	2.965	28.27
547.8	65.70	160.8	10.36	3.849	3.033	29.12
555.8	64.83	160.8	10.52	3.873	3.096	29.99
563.8	64.05	159.8	10.66	3.896	3.154	30.85
571.8	63.37	160.8	10.80	3.915	3.206	31.73
579.8	62.78	160.8	10.91	3.933	3.253	32.62
587.8	62.24	160.8	11.02	3.949	3.297	33.51
595.8	61.75	160.8	11.13	3.964	3.337	34.41
603.8	61.27	160.8	11.23	3.978	3.377	35.31
611.8	60.77	161.8	11.33	3.994	3.420	36.23
619.8	60.25	160.8	11.45	4.010	3.466	37.14
627.8	59.70	164.8	11.57	4.027	3.515	38.06
635.8	59.11	164.8	11.71	4.046	3.569	38.99
643.8	58.49	161.8	11.85	4.067	3.628	39.92
651.8	57.81	173.9	12.01	4.089	3.693	40.85
659.8	57.09	175.9	12.19	4.113	3.766	41.78
667.8	56.33	175.9	12.39	4.140	3.844	42.72
675.8	55.52	176.9	12.60	4.168	3.931	43.65
683.8	54.69	176.9	12.83	4.198	4.023	44.59
691.7	53.86	176.9	13.07	4.228	4.119	45.53
699.8	53.05	185.9	13.31	4.259	4.216	46.47

INTENTIONALLY LEFT BLANK.

No of Copies	Organization	No of Copies	Organization
2	Administrator Defense Technical Info Center ATTN: DTIC-DDA Cameron Station Alexandria, VA 22304-6145	1	Director US Army Aviation Research and Technology Activity ATTN: SAVRT-R (Library) M/S 219-3 Ames Research Center Moffett Field, CA 94035-1000
1	HQDA (SARD-TR) WASH DC 20310-0001	1	Commander US Army Missile Command ATTN: AMSMI-RD-CS-R (DOC) Redstone Arsenal, AL 35898-5010
1	Commander US Army Materiel Command ATTN: AMCDRA-ST 5001 Eisenhower Avenue Alexandria, VA 22333-0001	1	Commander US Army Tank-Automotive Command ATTN: AMSTA-TSL (Technical Library) Warren, MI 48397-5000
1	Commander US Army Laboratory Command ATTN: AMSLC-DL Adelphi, MD 20783-1145	1	Director US Army TRADOC Analysis Command ATTN: ATRC-WSR White Sands Missile Range, NM 88002-5502
2	Commander US Army, ARDEC ATTN: SMCAR-IMI-I Picatinny Arsenal, NJ 07806-5000	(Class. only) 1	Commandant US Army Infantry School ATTN: ATSH-CD (Security Mgr.) Fort Benning, GA 31905-5660
2	Commander US Army, ARDEC ATTN: SMCAR-TDC Picatinny Arsenal, NJ 07806-5000	(Unclass. only) 1	Commandant US Army Infantry School ATTN: ATSH-CD-CSO-OR Fort Benning, GA 31905-5660
1	Director Benet Weapons Laboratory US Army, ARDEC ATTN: SMCAR-CCB-TL Watervliet, NY 12189-4050	1	Air Force Armament Laboratory ATTN: AFATL/DLODL Eglin AFB, FL 32542-5000
1	Commander US Army Armament, Munitions and Chemical Command ATTN: SMCAR-ESP-L Rock Island, IL 61299-5000		<u>Aberdeen Proving Ground</u>
1	Commander US Army Aviation Systems Command ATTN: AMSAV-DACL 4300 Goodfellow Blvd. St. Louis, MO 63120-1798	2	Dir, USAMSAA ATTN: AMXSY-D AMXSY-MP, H. Cohen
		1	Cdr, USATECOM ATTN: AMSTE-TD
		3	Cdr, CRDEC, AMCCOM ATTN: SMCCR-RSP-A SMCCR-MU SMCCR-MSI
		1	Dir, VLAMO ATTN: AMSLC-VL-D

No. of  
Copies   Organization

- 5   Commander  
US Army, ARDEC  
ATTN: SMCAR-FSA-E,  
Dr. T. Gora  
John Bennett  
SMCAR-AEE-B,  
Dr. D. Downs  
SMCAR-CCL-FA,  
H. Moore  
H. Kahn  
Picatinny Arsenal, NJ 07806-5000
- 2   Director  
Benet Weapons Laboratory  
US Army, ARDEC  
ATTN: SMCAR-CCB-DS,  
Dr. C. A. Andrade  
SMCAR-CCB-RM,  
Dr. Pat Vottis  
Watervliet, NY 12189
- 1   Director  
DARPA  
ATTN: Dr. Peter Kemmey  
1400 Wilson Blvd.  
Arlington, VA 22209
- 1   Commander  
SDIO  
ATTN: SDIO/IST,  
MAJ M. Huebschman  
Washington, DC 20301-7100
- 4   CG, MCRDAC  
Code AWT  
ATTN: Dr. C. Vaughn  
Mr. C. Childers  
MAJ R. Jensen  
Mr. G. Solhand  
Quantico, VA 22134-5080
- 1   Director  
US Army Research Office  
ATTN: Dr. Michael Ciftan  
P. O. Box 12211  
Research Triangle Park, NC 27709-2211

No. of  
Copies   Organization

- 2   Air Force Armament Laboratory  
ATTN: AFATL/DLJG,  
Mr. Kenneth Cobb  
AFATL/DLDG,  
Dr. T. Aden  
Eglin AFB, FL 32542-5000
- 1   Director  
Brookhaven National Laboratory  
ATTN: Dr. J. R. Powell  
Bldg 129  
Upton, NY 11973
- 1   Director  
Lawrence Livermore National Laboratory  
ATTN: Dr. R. S. Hawke, L-156  
P. O. Box 808  
Livermore, CA 94550
- 3   Director  
Los Alamos National Laboratory  
ATTN: MSG 787,  
Mr. Max Fowler  
Dr. J. V. Parker  
Dr. William Condit  
Los Alamos, NM 87545
- 1   Sandia National Laboratory  
ATTN: Dr. Maynard Cowan  
Dept. 1220  
P. O. Box 5800  
Albuquerque, NM 87185
- 1   NASA Lewis Research Center  
ATTN: MS 501-7, Lynette Zana  
2100 Brook Park Road  
Cleveland, OH 44135
- 1   Astron Research & Engineering  
ATTN: Dr. Charles Powars  
130 Kifer Court  
Sunnyvale, CA 94086
- 2   Austin Research Associates  
ATTN: Dr. Millard L. Sloan  
Dr. William E. Drummond  
1091 Rutland Drive  
Austin, TX 78758



<u>No. of Copies</u>	<u>Organization</u>
3	Maxwell Laboratories ATTN: Dr. Rolf Dethlefsen Dr. Ian McNab Dr. Mark Wilkinson 8888 Balboa Avenue San Diego, CA 92123
1	Boeing Aerospace Company ATTN: Dr. J. E. Shrader P. O. Box 3999 Seattle, WA 98134
2	GA Technologies, Inc. ATTN: Dr. Robert Bourque Dr. L. Holland P. O. Box 85608 San Diego, CA 92138
2	GT Devices ATTN: Dr. Shyke Goldstein Dr. D. Tidman 5705-A General Washington Drive Alexandria, VA 22312
1	General Dynamics ATTN: Dr. Jaime Cuadros P. O. Box 2507 Pomona, CA 91766
2	Electromagnetic Research, Inc. ATTN: Dr. Henry Kolm Dr. Peter Mongeau 2 Fox Road Hudson, MA 01749
2	General Electric Company (AEPD) ATTN: Dr. William Bird Dr. Slade L. Carr R D. #3, Plains Road Ballston Spa, NY 12020
1	General Research Corporation ATTN: Dr. William Isbell P. O. Box 6770 Santa Barbara, CA 93160-6770

<u>No. of Copies</u>	<u>Organization</u>
2	IAP Research, Inc. ATTN: Dr. John P. Barber Mr. David P. Bauer 2763 Culver Avenue Dayton, OH 45429-3723
2	LTV Aerospace & Defense Company ATTN: MS TH-83, Dr. Michael M. Tower Dr. C. H. Haight P. O. Box 650003 Dallas, TX 75265-0003
1	Pacific-Sierra Research Corp. ATTN: Dr. Genc E. McClellan 1401 Wilson Blvd. Arlington, VA 22209
1	R&D Associates ATTN: Dr. Peter Turchi P. O. Box 9695 Marina del Rey, CA 90291
1	Science Applications International Corporation ATTN: Dr. K. A. Jamison 1247-B North Eglin Parkway Shalimar, FL 32579
3	Science Applications International Corporation ATTN: Dr. Jad H. Batteh Dr. G. Rolader Mr. L. Thornhill 1503 Johnson Ferry Rd., Suite 100 Marietta, GA 30062
1	System Planning Corporation ATTN: Donald E. Shaw 1500 Wilson Blvd. Arlington, VA 22209
1	Westinghouse Electric Corporation Marine Division ATTN: Dr. Dan Omry 401 East Hendy Avenue Sunnyvale, CA 94088-3499

<u>No. of Copies</u>	<u>Organization</u>
2	Westinghouse Science and Technology Center ATTN: Dr. Bruce Swanson Mr. Doug Fikse 1310 Beulah Road Pittsburgh, PA 15233
2	Auburn University ATTN: Dr. Raymond F. Askew, Leach Nuclear Science Center Dr. E. J. Clothiaux, Department of Physics Auburn University, AL 36849-3501
1	Texas Technical University Department of EE/Computer Science ATTN: Dr. M. Kristiansen Lubbock, TX 79409-4439
1	Tuskegee Institute Dept. of Mechanical Engineering ATTN: Dr. Pradosh Ray Tuskegee Institute, AL 36088
1	University of Alabama in Huntsville School of Science & Engineering ATTN: Dr. C. H. Chen Huntsville, AL 35899
1	University of Miami ATTN: Dr. Manuel A. Huerta, Physics Dept. P.O. Box 248046 Coral Gables, FL 33124
1	University of Tennessee Space Institute ATTN: Dr. Dennis Keefer Tullahoma, TN 37388-8897
3	University of Texas Center for Electromechanics Balcones Research Center ATTN: Mr. William Weldon Mr. Raymond Zaworka Dr. Harry Fair 10100 Burnet Road, Bldg. 133 Austin, TX 78748

<u>No. of Copies</u>	<u>Organization</u>
1	Dr. E. W. Sucov 1065 Lyndhurst Drive Pittsburgh, PA 15206
2	SPARTA Inc. ATTN: Jeffery Kezerian Dr. Michael M. Holland 9455 Towne Centre Drive San Diego, CA 92121-1964
1	Supercon Inc. ATTN: Charles Renaud 830 Boston Turnpike Road Shrewsbury, MA 01545
	<u>Aberdeen Proving Ground</u>
1	Cdr, USATECOM ATTN: AMSTE-SI-F

## USER EVALUATION SHEET/CHANGE OF ADDRESS

This Laboratory undertakes a continuing effort to improve the quality of the reports it publishes. Your comments/answers to the items/questions below will aid us in our efforts.

1. BRL Report Number BRL-TR-3175 Date of Report NOVEMBER 1990

2. Date Report Received \_\_\_\_\_

3. Does this report satisfy a need? (Comment on purpose, related project, or other area of interest for which the report will be used.) \_\_\_\_\_  
\_\_\_\_\_  
\_\_\_\_\_

4. Specifically, how is the report being used? (Information source, design data, procedure, source of ideas, etc.) \_\_\_\_\_  
\_\_\_\_\_  
\_\_\_\_\_

5. Has the information in this report led to any quantitative savings as far as man-hours or dollars saved, operating costs avoided, or efficiencies achieved, etc? If so, please elaborate. \_\_\_\_\_  
\_\_\_\_\_  
\_\_\_\_\_

6. General Comments. What do you think should be changed to improve future reports? (Indicate changes to organization, technical content, format, etc.) \_\_\_\_\_  
\_\_\_\_\_  
\_\_\_\_\_  
\_\_\_\_\_  
\_\_\_\_\_

CURRENT  
ADDRESS

\_\_\_\_\_  
Name  
\_\_\_\_\_  
Organization  
\_\_\_\_\_  
Address  
\_\_\_\_\_  
City, State, Zip Code

7. If indicating a Change of Address or Address Correction, please provide the New or Correct Address in Block 6 above and the Old or Incorrect address below.

OLD  
ADDRESS

\_\_\_\_\_  
Name  
\_\_\_\_\_  
Organization  
\_\_\_\_\_  
Address  
\_\_\_\_\_  
City, State, Zip Code

(Remove this sheet, fold as indicated, staple or tape closed, and mail.)

-----FOLD HERE-----

**DEPARTMENT OF THE ARMY**

Director

U.S. Army Ballistic Research Laboratory

ATTN: SLCBR-DD-T

Aberdeen Proving Ground, MD 21005-5066

**OFFICIAL BUSINESS**



NO POSTAGE  
NECESSARY  
IF MAILED  
IN THE  
UNITED STATES

**BUSINESS REPLY MAIL**  
FIRST CLASS PERMIT No 0001, APG, MD

POSTAGE WILL BE PAID BY ADDRESSEE

Director

U.S. Army Ballistic Research Laboratory

ATTN: SLCBR-DD-T

Aberdeen Proving Ground, MD 21005-9989



-----FOLD HERE-----